





Cite this: *RSC Adv.*, 2023, 13, 19585

# The controllable synthesis of NiO/Ni/C nanosheets via pulsed plasma in ethylene glycol solution for oxygen evolution electrocatalysis†

Rong Tu, <sup>abc</sup> Kunqiu Leng,<sup>ab</sup> Chao Song,<sup>d</sup> Chitengfei Zhang, <sup>\*eab</sup>  
Yingqiu Zheng,<sup>ab</sup> Yuzhe Han,<sup>a</sup> Guoqiang Luo,<sup>ab</sup> Song Zhang <sup>abe</sup> and Takashi Goto<sup>a</sup>

NiO-based composites exhibit high catalytic activity for the oxygen evolution reaction (OER). Herein, high-performance NiO/Ni/C nanosheet catalysts were obtained by liquid-phase pulsed plasma (LPP), which was generated between two nickel electrodes in ethylene glycol (EG) solution by a homemade high-voltage pulse power supply. Melted nickel nanodrops were ejected from nickel electrodes which were bombarded by the energetic plasma. Simultaneously, high-temperature nickel nanodrops promoted the decomposition of the organics which were converted in the EG solution by the catalysis of LPP and formed hierarchical porous carbon nanosheets. Due to the high surface energy of the hierarchical porous carbon nanosheets, the spherical particles of Ni/NiO were adsorbed on the surface to compose the NiO/Ni/C composites. The pore size distribution of the composites could be controlled with different EG concentrations. When the EG concentration was 10 vol% (EG30), the composites possessed a H2 + H2 + H3 type pore size distribution and maximum active site area, leading to an exceptional OER activity (289.2 mV overpotential at 10 mA cm<sup>-2</sup>).

Received 17th April 2023  
Accepted 22nd June 2023

DOI: 10.1039/d3ra02544f

rsc.li/rsc-advances

## 1. Introduction

The water-splitting process is regarded as a highly promising method for hydrogen synthesis, given its non-toxic and non-polluting characteristics, in contrast to conventional hydrogen production technologies.<sup>1,2</sup> The electrocatalytic water-splitting process involves a cathodic hydrogen evolution reaction (HER) and an anodic oxygen evolution reaction (OER). Essentially, OER is a four-proton coupled electron transfer process, demanding a higher energy to overcome its kinetic barrier compared to HER.<sup>3</sup> Therefore, the development of efficient OER catalysts is crucial for enhancing the energy efficiency of water splitting. Generally, noble-metal oxide (e.g., IrO<sub>2</sub> and RuO<sub>2</sub>) catalysts exhibit outstanding OER catalytic activity, however, their limited availability and expense restrict their practical use in wide-ranging industrial applications.<sup>4,5</sup> It has been found that transition metal oxide-based compounds also exhibit

excellent OER catalytic activity, especially the low-cost and abundant NiO-based materials.<sup>6–8</sup> However, the low electrical conductivity of pure NiO is not conducive to electron transport, limiting its OER performance. Therefore, combining NiO with other conductive materials (such as C and Ni) is a highly effective approach for improving its OER performance.

Currently, various methods have been used to modify NiO-based catalysts, such as chemical vapor deposition (CVD),<sup>9</sup> hydrothermal,<sup>10</sup> aqueous solution blow spinning,<sup>11</sup> CVD method is capable of producing single-phase catalysts with controllable size and morphology. But it is difficult for CVD method to synthesize multiphase catalysts with complex structure, unless pre- or post-processing is performed. Hydrothermal method involves multi-step process, high-temperature, high-pressure and several-hours reaction time. The aqueous solution – blowing method usually has uneven fiber diameters and weak bonding between fiber attachments and fibers, resulting in unstable OER performance tests. In contrast, the LPP method is a one-step synthesis reaction that can be achieved under standard temperature and pressure conditions, with a shorter reaction time.<sup>12</sup> And the nonequilibrium plasma, short discharge time and the quenching effect of the surrounding cooling solution restrict the critical size of the crystals, resulting in the synthesis of atomic-scale catalysts. Furthermore, a wide variety of nanomaterials could be obtained by changing the dielectric solution and electrodes, such as metal,<sup>13–19</sup> nitrides,<sup>20</sup> carbides,<sup>21</sup> oxides nanoparticles,<sup>22–24</sup> core-shell and/or onion-like nanomaterials.<sup>25–27</sup> Most of the raw materials in the

<sup>a</sup>Chaozhou Branch of Chemistry and Chemical Engineering Guangdong Laboratory, Chaozhou 521000, China

<sup>b</sup>State Key Laboratory of Advanced Technology for Materials Synthesis and Processing, Wuhan University of Technology, Wuhan 430070, China

<sup>c</sup>Wuhan University of Technology, Advanced Engineering Technology Research Institute of Zhongshan City, Zhongshan 528400, China

<sup>d</sup>School of Materials Science and Engineering, Hanchuan Normal University, Chaozhou 521041, China

<sup>e</sup>Hubei Longzhong Laboratory, Xiangyang 441000, China

† Electronic supplementary information (ESI) available. See DOI: <https://doi.org/10.1039/d3ra02544f>


previous literature are metal salts, which are reduced by plasma and form atomic-scale catalysts. However, the high conductivity of the metal salt solution can quickly lead to electrode breakdown and cause short circuits, which is not conducive to the formation of plasma.

In this study, nickel rods instead of nickel salt were used as nickel source, and solvent-ethylene glycol solution was served as discharge solution, carbon source and reducing agent.<sup>28</sup> And the effects of the composition and microstructure of the NiO/Ni/C nanosheets on the OER performance were investigated. The EG30 presented a remarkable OER performance with the overpotential of 289.2 mV at 10 mA cm<sup>-2</sup>, indicating their great potential as an OER catalyst in oxygen production by the water-splitting.

## 2. Experimental

### 2.1 Synthesis of NiO/Ni/C nanosheets

The schematic diagram of the experimental setup for the synthesis of NiO/Ni/C nanosheets is shown in Fig. 1. Two nickel metal rods (Xiu'ao Metal Materials Co., Ltd China) with a diameter of 6 mm, a length of 250 mm, and 99.99% in purity were used as electrodes. The distance between the two nickel electrode rods (cathode and anode) was less than 0.5 mm. Pulsed electrical discharge was generated in liquid by a high-voltage pulse power supply with the applied voltage, pulse width, and frequency of 4 kV, 300 ns, and 3 kHz, respectively. The total volume of EG (Beijing Innochem Technology Co., Ltd, 99%) and deionized water was 300 ml. Content of EG solutions for each sample are shown in Table 1.

### 2.2 Characterization

X-ray diffraction (XRD) patterns were collected by a SmartLab X-ray diffractometer (Cu K $\alpha$ , Rigaku, Japan). Raman spectra were acquired using a confocal Raman microscope (inVia<sup>TM</sup>, Renishaw, UK) with 532 nm laser excitation. Morphology and nanostructure were characterized by a field emission scanning electron microscopy (FESEM, Regulus8100, Japan) and a high-resolution transmission electron microscopy (HR-

Table 1 Content of EG solutions for each sample

Sample	EG volume (mL)	Deionized water volume (mL)
EG0	0	300
EG10	10	290
EG30	30	270
EG50	50	250
EG70	70	230
EG90	90	210

TEM, FEI Talos-F200S, USA). The chemical states were analyzed by an X-ray photoelectron spectroscopy (XPS, Thermo Fisher Scientific, USA) technique. Nitrogen adsorption and desorption isotherms were measured by a Micromeritics Instruments ASAP 2020 nitrogen adsorption apparatus. The Barrett-Joyner-Halenda (BJH) method was utilized to determine the pore size distribution. The component analysis of as-prepared solution was detected by the gas chromatography-mass spectrometry (GC-MS, Agilent 7890B, USA).

### 2.3 Electrocatalysis measurement

A three-electrode electrochemical workstation (Wuhan CorrTest Instruments Corp., Ltd, CS2350H, China) was used for all electrochemical measurements. To prepare the catalytic slurry, a 4 mg powder sample was mixed with 50  $\mu$ L Nafion (Dupont, 5 wt%), and then dispersed in a mixture of 375  $\mu$ L ultrapure water and 125  $\mu$ L ethanol (98%, Sinopharm Chemical Reagent). The counter electrode was a graphite electrode, while a saturated Hg/HgO electrode (Tianjin Aida Hengsheng Technology Development Co., Ltd, R0501) was used as the reference electrode.

Linear sweep voltammetry (LSV) polarization curves were obtained at a scan rate of 2 mV s<sup>-1</sup> in a potential range of 0.18–0.78 V (vs. Hg/HgO). The double-layer capacitance ( $C_{dl}$ ) was determined *via* cyclic voltammetry (CV) across non-faradaic potential regions using varying scan rates (10, 20, 30, 40, 50, and 60 mV s<sup>-1</sup>). The electrochemical active surface areas (ECSA)

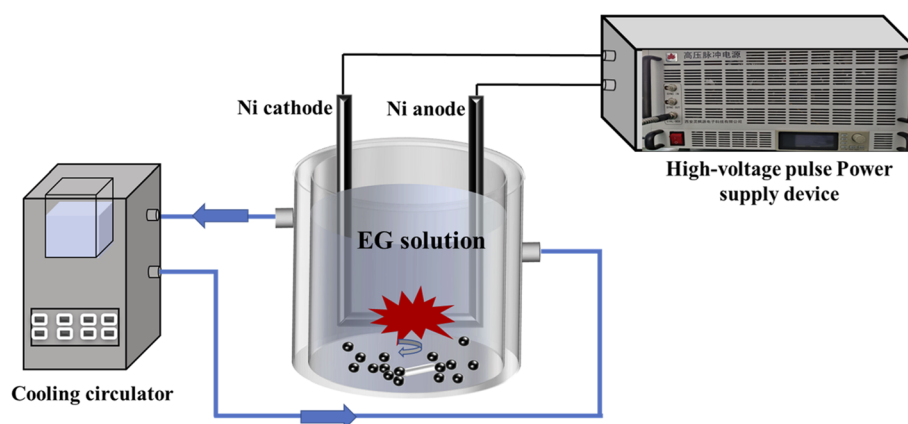


Fig. 1 The Schematic of the liquid-phase pulsed plasma method.



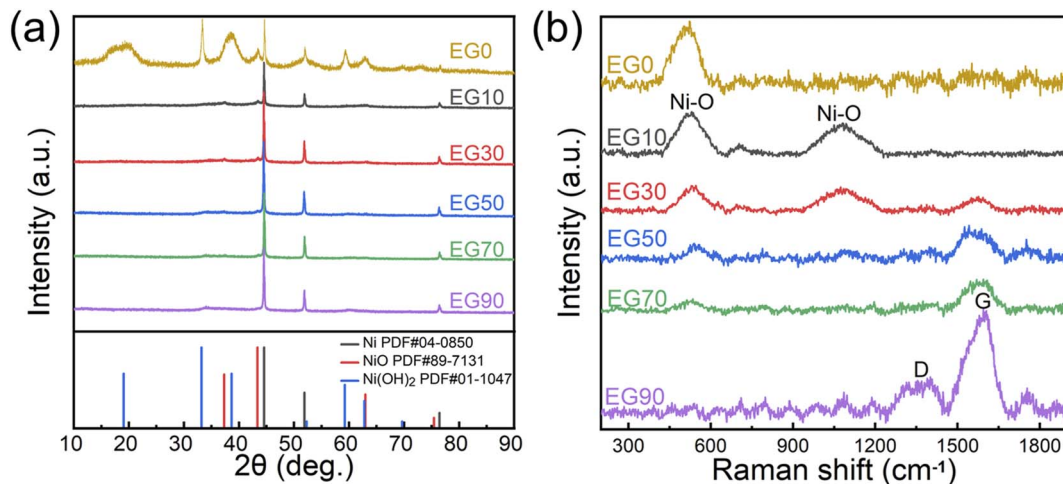


Fig. 2 XRD patterns (a) and Raman spectra (b) of EG0, EG10, EG30, EG50, EG70, and EG90 samples.

were determined by calculating the  $C_{dl}$  values. Nyquist plots were obtained through electrochemical impedance spectroscopy (EIS), using an AC signal with a frequency range of 0.1 Hz to 100 kHz and a voltage amplitude of 5 mV, applied at open circuit potential. The potentials relative to Hg/HgO were converted to those relative to reversible hydrogen electrodes (RHE) using the Nernst equation, which is given by  $E_{RHE} = E_{Hg/HgO} + 0.098 + 0.059 \times \text{pH}$ . The overpotential  $\eta = E_{RHE} - 1.23$  V. IR compensation set to 95%.

### 3. Results and discussion

#### 3.1 Crystal phase

The figures, including Fig. 2a, and b, collectively demonstrate that the relative content of NiO is inversely proportional to the concentration of EG. As demonstrated in XRD pattern (Fig. 2a), three intensive diffraction peaks at 44.5°, 51.8°, and 76.3° are indexed to (111), (200), and (220) crystal planes of cubic Ni (PDF#04-0850), respectively. Three weak diffraction peaks at

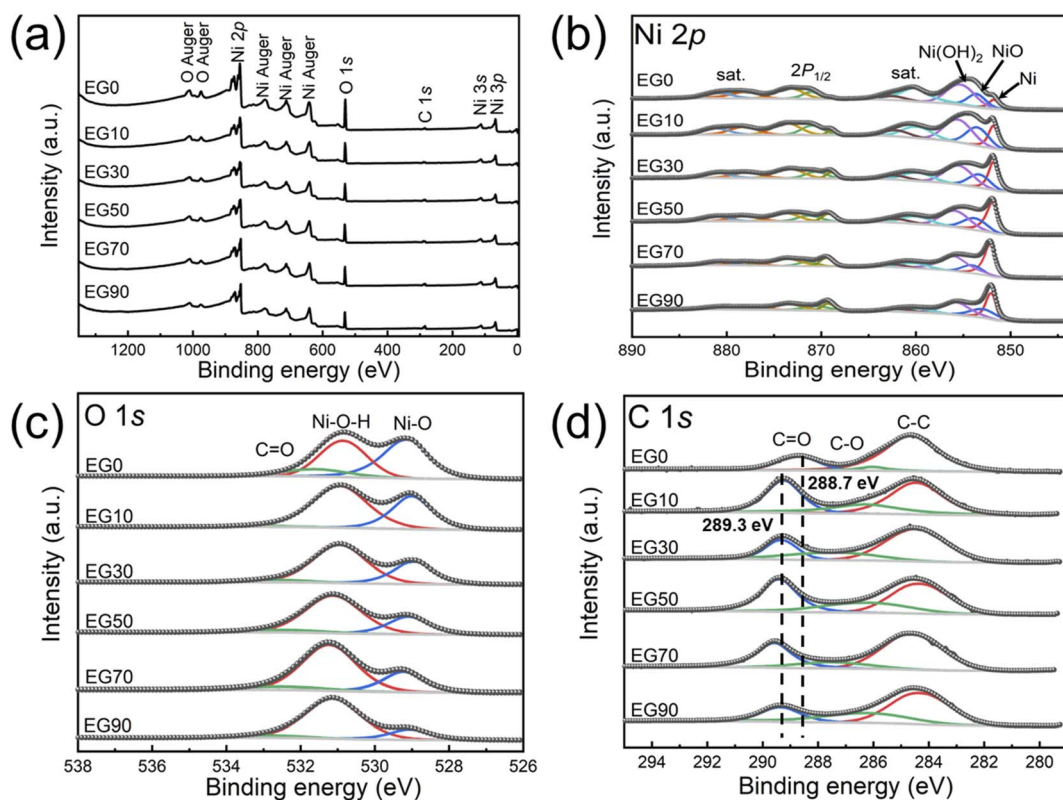


Fig. 3 XPS spectra of EG0, EG10, EG30, EG50, EG70, and EG90 for (a) survey; (b) Ni 2p; (c) O 1s; (d) C 1s.



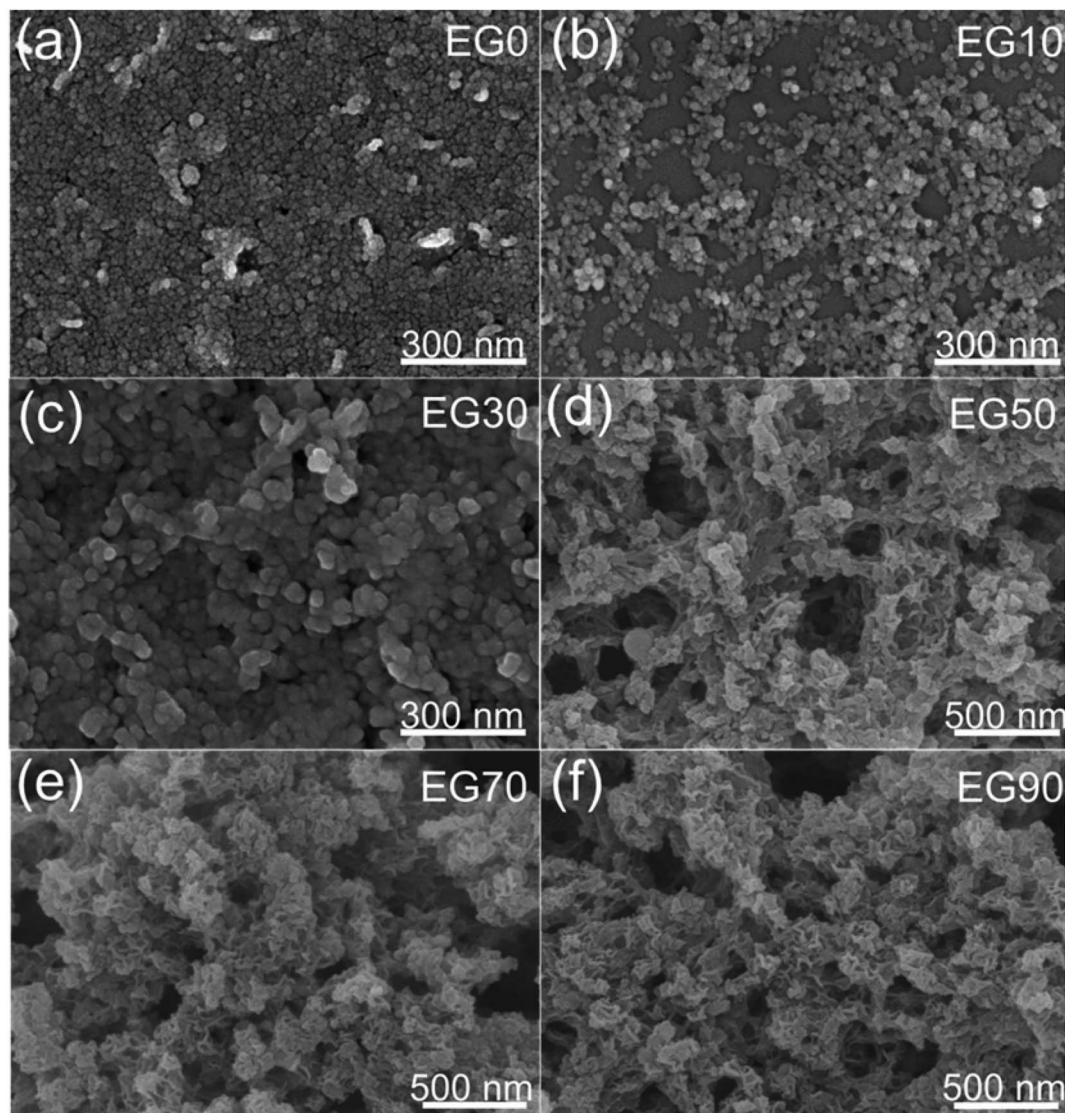


Fig. 4 FESEM images of EG0 (a), EG10 (b), EG30 (c), EG50 (d), EG70 (e), and EG90 (f).

37.2°, 43.3°, and 62.9° are associated with (110), ( $\bar{1}11$ ), and (111) crystal planes of monoclinic NiO (PDF#89-7131). Five diffraction peaks at 18.9°, 33.2°, 38.6°, 59.2°, and 62.7° correspond to the (001), (100), (101), (110) and (111) crystal planes of hexagonal Ni(OH)<sub>2</sub> (PDF#01-1047), respectively. Without EG in solution (EG0), the high-temperature nickel particles eroded by the pulsed plasma are oxidized to Ni(OH)<sub>2</sub> and NiO by water. While, with EG in solution, the hydroxyl groups in EG could protect the nickel-molten drops from oxidation.<sup>28</sup>

Fig. 2b depicts the Raman spectra of EG0, EG10, EG30, EG50, EG70, and EG90. The two peaks centered at 510 and 1080 cm<sup>-1</sup> correspond to the stretching vibrations of the Ni–O bond, while the D band at around 1350 cm<sup>-1</sup> and G band at 1590 cm<sup>-1</sup> are attributed to the disordered carbon and graphitic structure, respectively.<sup>29</sup> The formation of carbon is related to the decomposition reaction of EG solution under the catalysis of high-temperature nickel particles and pulsed plasma. Thus, the

relative content of carbon is directly proportional to the concentration of EG.

The XPS spectra of Fig. 3 reveal the elemental composition and valence of the EG0, EG10, EG30, EG50, EG70, and EG90. The XPS spectra presented in Fig. 3a validate the presence of Ni, C, and O in the samples. As depicted in the spectra of Ni 2p (Fig. 3b), multiple-split peaks at approximately 853.7 and 855.6 eV which belong to Ni 2p<sub>3/2</sub> indicate the existence of NiO and Ni(OH)<sub>2</sub>, respectively,<sup>9</sup> and the multiple-split peaks at the binding energy of 852.1 eV suggest the existence of Ni<sup>0</sup>.<sup>30</sup> Due to the partially incompletely reduced Ni(OH)<sub>2</sub> in EG10, EG30, EG50, EG70, and EG90, the binding energy around 855 eV has not disappeared. Furthermore, the relative intensity of the Ni<sup>0</sup> peak is gradually stronger with the increase of the EG concentration which is in contrast to the peak of NiO and Ni(OH)<sub>2</sub>. The three peaks at the binding energies 529.6, 531.7, and 533.4 eV in the O 1s spectra (Fig. 3c) are respectively assigned to Ni–O bond,



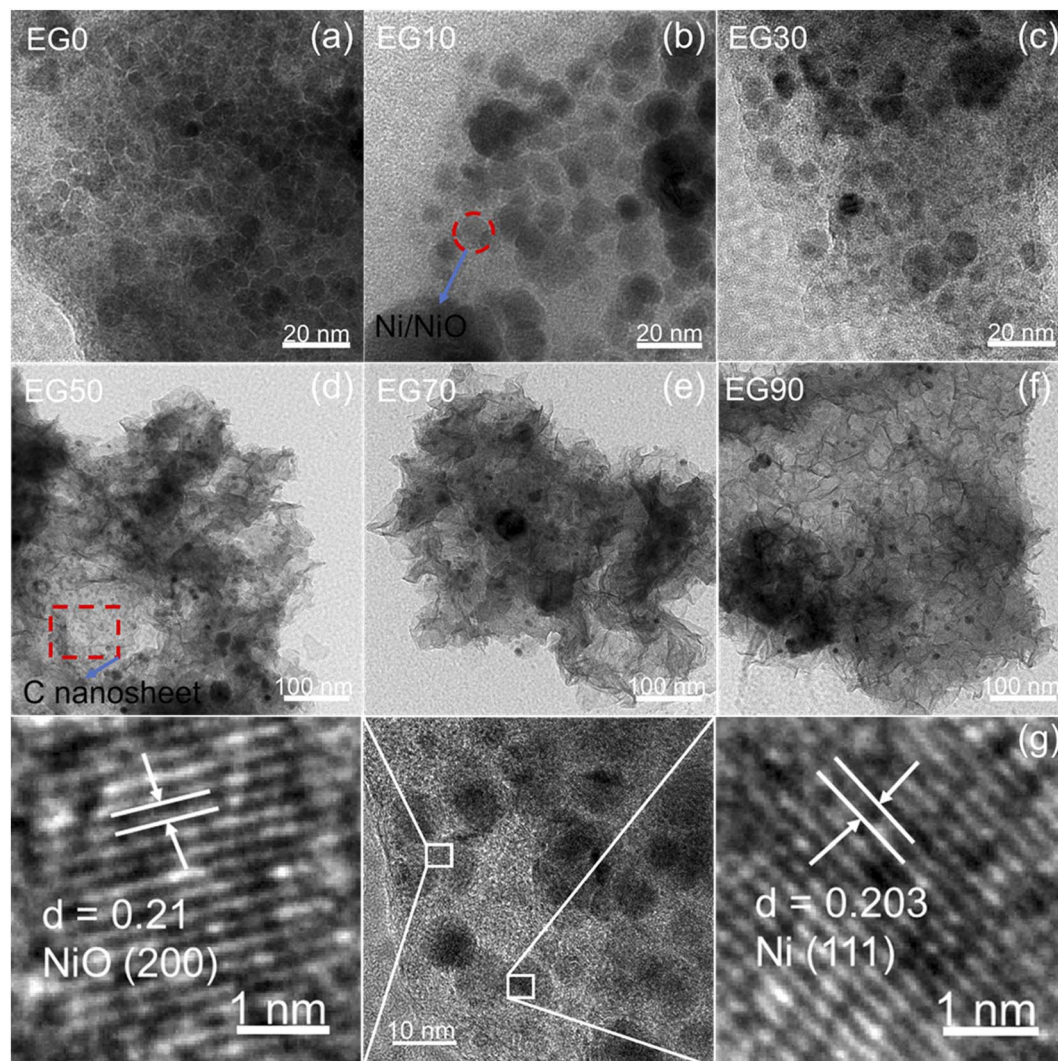


Fig. 5 TEM images of (a) EG0, (b) EG10, (c) EG30, (d) EG50, (e) EG70, (f) EG90, and (g) HRTEM image of EG30.

Ni–O–H bond, and C=O bond. The three peaks at the binding energies 284.8, 286.3, and around 289 eV in the C 1s spectra (Fig. 3d) are correlated to the C–C bond, C–O bond, and C=O bond, respectively.<sup>9</sup> Compared with the C=O peak of EG0 (288.7 eV), the peaks of EG10, EG30, EG50, EG70, and EG90 shifted to 289.3 eV due to the effect of C and Ni/NiO.

### 3.2 Microstructure

Fig. 4a–c respectively display the as-prepared FESEM images EG0, EG10, and EG30, revealing the morphology of the spherical nanoparticles, suggesting that the EG10 sample has the best particle dispersion. As the concentration of EG increased, wrinkled sheet-like structures appeared, as shown in Fig. 4d–f. The structure and morphology of the as-prepared samples are further revealed by HRTEM in Fig. 5. The images of Fig. 5d–f reveal that sheet-like wrinkled morphology exists in EG50, EG70, and EG90 samples, and spherical particles are dispersed to these nanosheets. Combining Raman and transmission analysis, nanosheets are carbon and spherical particles are Ni/NiO. As displayed in Fig. 5g, two sets of lattice fringes with

spacings of 0.203 and 0.21 nm are observed, corresponding to the (111) and (200) planes of Ni and NiO, respectively.

N<sub>2</sub> adsorption–desorption isotherms provide information on the specific surface area ( $S_{\text{BET}}$ ). Fig. 6 demonstrates distinctive type IV isotherms with hysteresis loops in all samples, indicating the presence of mesopores.<sup>31</sup> The hysteresis loop of EG0 and EG10 (Fig. 6a and b) are an overlap hysteresis loop of H2 and H3.<sup>31</sup> Attributing to the accumulation of spherical particles in Fig. 4a and b, the steep hysteresis loop in the desorption branch at a relative pressure ( $P/P_0$ ) ranging from 0.4–0.9 is the feature of the type-H2 hysteresis loop, indicating the presence of ink-bottle shape pores.<sup>32</sup> And the inconspicuous hysteresis loop of the desorption branch at a relative pressure of 0.9–1.0 corresponds to the type-H3 hysteresis loop. As displayed in Fig. 6c, the isotherms of EG30 consist of three parts hysteresis loops, which corresponds to the type-H2 loops ( $P/P_0 = 0.4–0.7$ , and  $P/P_0 = 0.7–0.9$ ), and the type of H3 loop ( $P/P_0 = 0.9–1.0$ ), respectively. The isotherm characteristics in Fig. 6d–f are similar, suggesting that the type of H2 and H3 hysteresis loops exist in EG50, EG70, and EG90. And the above results of BET are





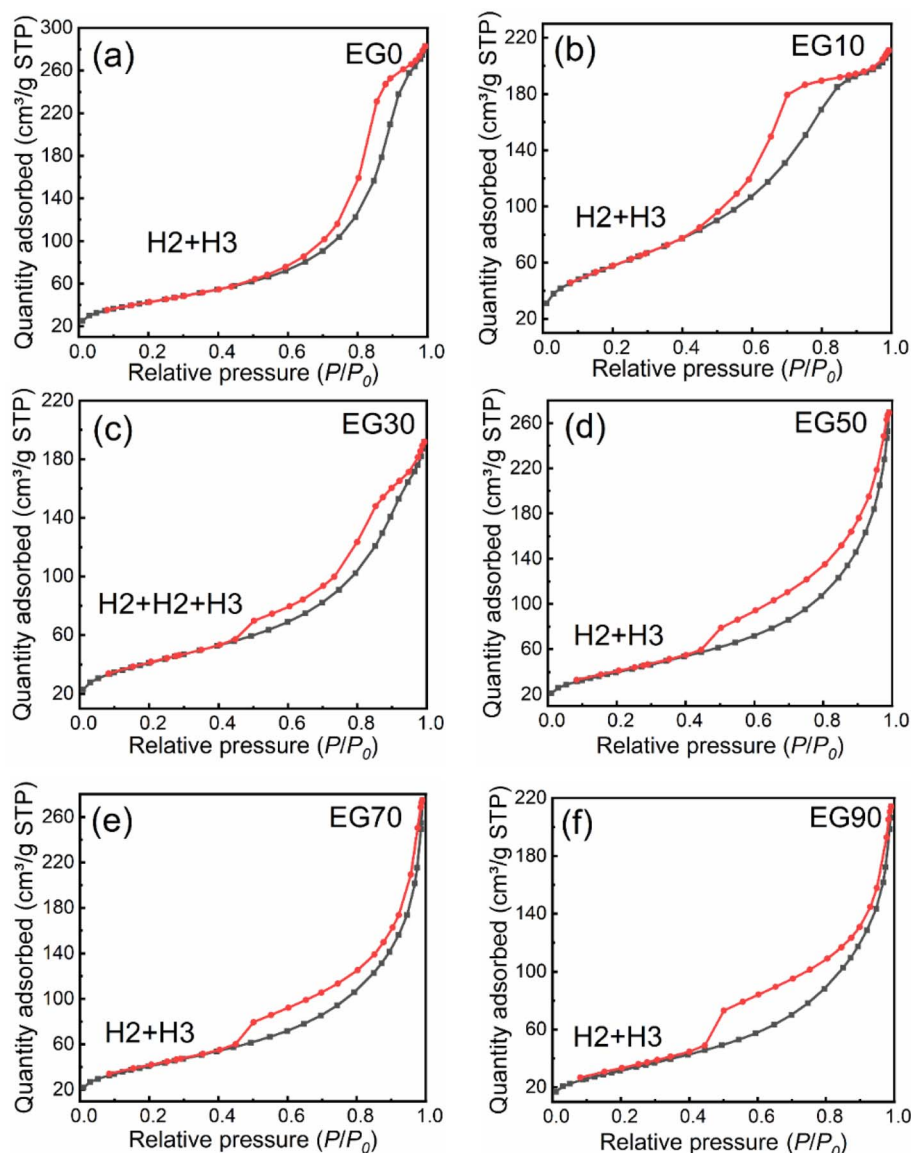


Fig. 6 Nitrogen adsorption-desorption isotherms obtained on sample EG0 (a), EG10 (b), EG30 (c), EG50 (d), EG70 (e), and EG90 (f).

consistent with SEM (Fig. 4a–f) and TEM (Fig. 5a–f) images, in which the appearance of type-H2 loop ascribes to the ink-bottle shape pores resulting from the accumulation of spherical particles, and the type-H3 hysteresis loop is derived from the narrow-slit shape pores formed by the stacked sheet-like structure. As revealed in Table S1,<sup>†</sup> The  $S_{\text{BET}}(\text{EG}_{10})$  is the largest, suggesting that the existence of carbon may reduce the  $S_{\text{BET}}$  of the samples.

High-voltage pulse liquid-phase discharge technology mainly generates plasma in water through high-voltage pulse current. The process can simultaneously generate shock waves, ultraviolet light, strong oxidizing free radicals, and strong electric fields.<sup>33</sup> In the liquid phase plasma, discharge plasma includes arc discharge plasma,<sup>34</sup> spark discharge plasma,<sup>35</sup> and/or corona streamer discharge plasma.<sup>36</sup> Streamer-like discharge results in a plasma channel that dissipates before spanning the entire electrode gap. Spark discharge produces temporary

conductive channels that bridge the gap between the electrodes, whereas arc discharge maintains the plasma channel spanning the electrodes for longer periods.<sup>37</sup> Therefore, the pulse plasma in this study might have been an arc discharge plasma, which possesses high energy and shorter discharge gap to erode the electrode.

The inset of Fig. 7 depicts the GC-MS spectrum of the as-prepared solution of the EG30 sample. The result demonstrates that the main composition of the as-prepared solution is ethyl acetate and may also contain small amounts of methanol or other organic compounds (Fig. S1 and Table S2<sup>†</sup>). Based on the above phase, structure, and GC-MS analysis, the formation mechanism of NiO/Ni/C nanosheets prepared by the liquid-phase pulsed plasma method is shown in Fig. 7.<sup>25</sup> First, EG was oxidized into acetic acid and other organic compounds by strong oxidizing free radicals under the influence of plasma. Furthermore, the EG could also be decomposed into ethanol



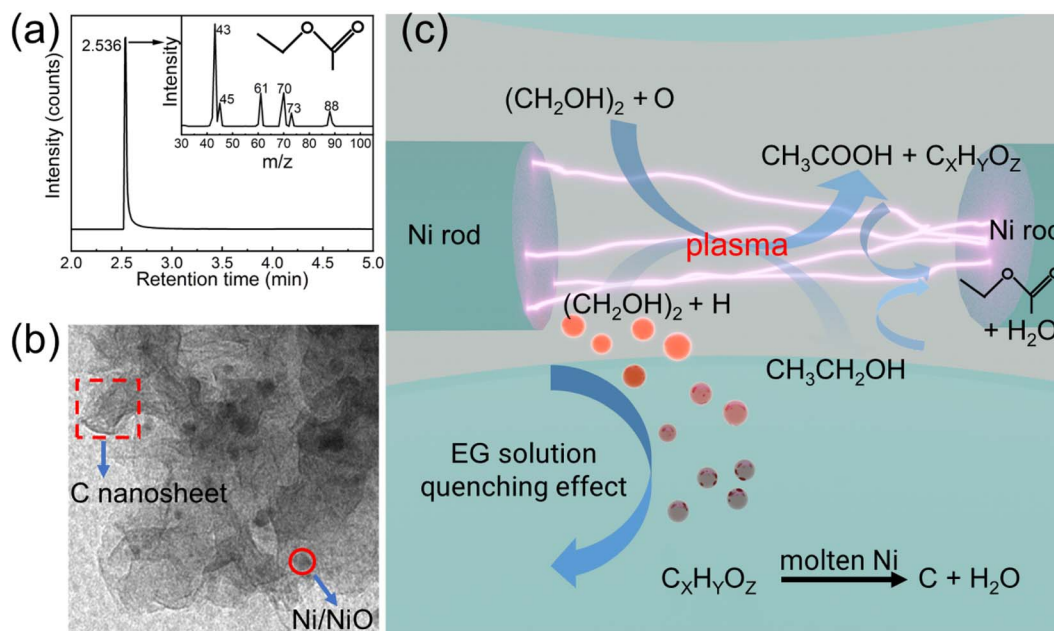


Fig. 7 Schematic formation mechanism of the NiO/Ni/C nanosheets.

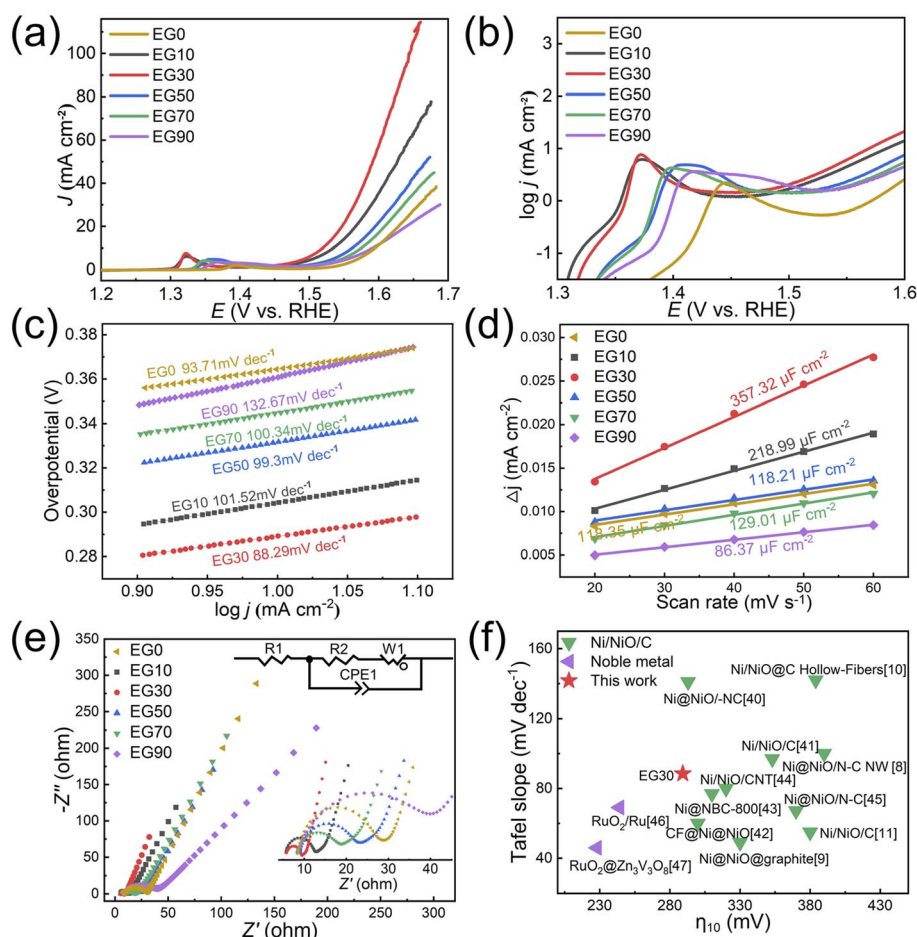


Fig. 8 (a) LSV plots, (b) enlargement of the (a) plot with the logarithm of the Y-axis, (c) Tafel curves, (d) double-layer capacitance at different scan rates ( $C_e = 0.04 \text{ mF cm}^{-2}$  in alkaline solutions), (e) EIS Nyquist plots, (f) Comparison of the overpotentials ( $\eta_{10}$ ) and Tafel slopes of the EG 30 (this work) with other electrocatalysts reported in prior literature.

under the influence of plasma. Then, ethanol and acetic acid reacted to form ethyl acetate. Simultaneously, the pulsed plasma eroded the nickel rod (Figs. S2a and b†) and formed a large amount of nickel molten nanodrops, similar to the process of multi-arc ion plating (Fig. S2c†). Then, the nickel molten nanodrops with high temperatures, as a catalyst, could promote the decomposition of the organic compounds in the solution into carbon nanosheets with abundant surface morphology. EG could protect also the nickel molten nanodrops from oxidation. Finally, NiO/Ni/C nanosheet was formed under the quenching effect of cooling EG solution.

### 3.3 OER performance

The OER properties of EG0, EG10, EG30, EG50, EG70, and EG90 prepared in this study are shown in Fig. 8, and the OER performance parameters are summarized in Table S3.† The LSV measurements (Fig. 8a) were carried out in 1 M KOH. The EG30 required the lowest overpotential (only 289.2 mV) at a current density of  $10 \text{ mA cm}^{-2}$ , exhibiting the best OER activity.

Fig. 8b depicts the  $\log j$  vs. overpotential image (plotted by taking the current density of Fig. 8a logarithmically), highlighting the oxidation peak in the electrochemical reaction. The formation of oxidation peak demonstrates that the  $\text{Ni(OH)}_2$  was converted into  $\text{NiOOH}$  during the electrocatalytic measurement. The conversion process is:  $\text{Ni(OH)}_2 \xrightarrow{\text{OH}^-} \text{NiOOH}$ . In alkaline media, two different hydroxides ( $\alpha\text{-Ni(OH)}_2$  and  $\beta\text{-Ni(OH)}_2$ ) can be formed on the surface of Ni and NiO. And both hydroxides are easily oxidized and form two different phases of  $\text{NiOOH}$ :  $\alpha\text{-Ni(OH)}_2 \xrightarrow{\text{OH}^-} \gamma\text{-NiOOH}$  and  $\beta\text{-Ni(OH)}_2 \xrightarrow{\text{OH}^-} \beta\text{-NiOOH}$ .<sup>9</sup> Broad oxidation peaks in EG50, EG70, and EG90 could be attributed to the relatively larger overpotential required for converting Ni to  $\text{NiOOH}$  compared to NiO.

Fig. 8c illustrates the Tafel plots used to explore the catalytic kinetics of the samples. In general, the smaller the Tafel slope is, the better the catalytic performance exhibited. As displayed in the graph, the EG30 exhibits the smallest Tafel slope, measuring  $88.29 \text{ mV dec}^{-1}$ . CV curves can provide electrochemical  $C_{\text{dl}}$  values within the potential range when the electrode/electrolyte solution interface exhibits non-faradaic behavior (Fig. 8d). According to the equation  $\text{ECSA} = C_{\text{dl}}/C_e$ , where  $C_e$  is the capacitance per unit area of the electrolyte and  $C_{\text{dl}}$  is the double-layer capacitance. In plotting the current density *versus* scan rate in the non-faradaic region,  $C_{\text{dl}}$  is obtained from the slope of the line. In general, ECSA primarily considers the electrochemically active sites, whereas BET quantifies all surface sites, encompassing both electrochemically active and inactive ones. Although the EG30 doesn't possess the largest  $S_{\text{BET}}$ , it shows the best catalytic performance with the largest ECSA.

Fig. 8e illustrates the EIS Nyquist plots of the samples, with the equivalent circuit diagram and zooming diagram presented in the inset. The image appears as a semicircle in the high-frequency region and as a straight line in the low-frequency region, which can be fitted to the curve using Zview software. The diameter of the Nyquist diagram's semi-circle corresponds to the charge transfer resistance  $R_{\text{ct}}$ , which exhibits an inverse relationship with the exchange current density of the

electrochemical process.  $R_2$  is the electrochemical reaction electron transfer impedance, equivalent to  $R_{\text{ct}}$ . The smaller the  $R_{\text{ct}}$  is, the smaller the electrochemical impedance is. The faster the electron transfer rate, the better the OER performance.  $R_1$  is the internal resistance of the solution, which usually refers to the internal resistance of the electrolyte between the reference electrode and the working electrode. CPE is the constant phase element and  $W_1$  is the Warburg element (open). Apparently, EG30 possesses the smallest  $R_{\text{ct}}$  and the fastest electron transfer rate, showing the best OER activity. The fitted EIS Nyquist plots are shown in the Fig. S3 and Table S4† presents the EIS fitted data table of different samples.

Fig. 8f summarizes the performance of the EG30 prepared in this study compared to the  $\text{NiO/Ni/C}^{8-10,38-44}$  and noble metal<sup>45,46</sup> previously reported in literature. Herein, we mainly compare overpotentials and Tafel slopes. Generally, for the OER, the smaller the overpotential and Tafel slope indicates the better the OER performance of the catalyst,<sup>47</sup> so the lower left-hand point in Fig. 8f is the better the performance. The overpotential of the as-prepared EG30 catalyst demonstrates comparable or superior performance in comparison to the  $\text{NiO/Ni/C}$  system. The overall OER performance of noble metal is superior to that of the  $\text{NiO/Ni/C}$  system.

In summary, EG30 exhibited the best OER performance. Although EG10 has the largest  $S_{\text{BET}}$ , it does not contain carbon, which plays a conductive role in the OER catalyst. Due to the formation of carbon sheets with abundant surface morphology, EG30 possesses a large  $S_{\text{BET}}$  and the largest ECSA. The H2 + H2 + H3 type porous size distribution in EG30 is beneficial for electron transport. All of these features have led to the best OER performance. In contrast to EG30, the decreased  $S_{\text{BET}}$  demonstrates that EG50, EG70, and EG90 have excessive carbon which covers the activity sites of the NiO, resulting in weakening the OER performance.

## 4. Conclusions

The pulsed plasma erodes the nickel rod and forms a large amount of high-temperature nickel molten nanodrops which could promote the decomposition of the organic compounds in the solution into carbon nanosheets. EG protects the nickel molten nanodrops from oxidation. By varying the concentration of EG, the morphology and structure of the resulting product can be tuned, ultimately resulting in the formation of  $\text{NiO/Ni/C}$  nanosheets. As the concentration of EG increases, the abundant surface morphology of carbon nanosheets appeared in the sample of EG50, EG70, and EG90. In contrast to the type of EG30 porous size distribution (H2 + H2 + H3), the other as-prepared samples possessed the H2 + H3 type. Comprehensive analysis shows that the best OER performance of EG30 is attributed to large  $S_{\text{BET}}$ , a certain amount of carbon, and the H2 + H2 + H3 type multi-level porous size distribution.

## Author contributions

Rong Tu: funding acquisition, conceptualization, methodology, writing – review & editing. Kunqiu Leng: formal analysis,





investigation, resources, data curation, writing – original draft. Chao Song: methodology, software, visualization. Chitengfei Zhang: conceptualization, methodology, formal analysis, writing – review & editing. Yingqiu Zheng: conceptualization, formal analysis. Yuzhe Han: validation, supervision. Guoqiang Luo: validation, funding acquisition. Song Zhang: software, project administration. Takashi Goto: software.

## Conflicts of interest

There are no conflicts to declare.

## Acknowledgements

This work was supported by the Guangdong Major Project of Basic and Applied Basic Research (2021B0301030001). It was also supported by the National Natural Science Foundation of China (No. 51861145306, 51872212, 51972244, 52002075 and 62204179), independent Innovation Projects of the Hubei Longzhong Laboratory (2022ZZ-06), the Key-Area Research and Development Program of Guangdong Province (2021B0707050001), the Self-innovation Research Funding Project of Hanjiang Laboratory (HJL202012A001, HJL202012A002, HJL202012A003) and the Major Science and Technology Project in Zhongshan City, Guangdong Province (2019AG029).

## References

- 1 X. Liu, X. Zhang, D.-S. Li, S. Zhang and Q. Zhang, *J. Mater. Chem. A*, 2021, **9**, 18164–18174.
- 2 H. Song, S. Luo, H. Huang, B. Deng and J. Ye, *ACS Energy Lett.*, 2022, **7**, 1043–1065.
- 3 M. I. James and M. Harb, *J. Energy Chem.*, 2021, **56**, 299–342.
- 4 S. M. Galani, A. Mondal, D. N. Srivastava and A. B. Panda, *Int. J. Hydrogen Energy*, 2020, **45**, 18635–18644.
- 5 Y. Hu, X. Luo, G. Wu, T. Chao, Z. Li, Y. Qu, H. Li, Y. Wu, B. Jiang and X. Hong, *ACS Appl. Mater. Interfaces*, 2019, **11**, 42298–42304.
- 6 K. Zhang and R. Zou, *Small*, 2021, **17**, 2100129.
- 7 A. Roy, M. Z. Tariq, M. La, D. Choi and S. J. Park, *J. Electroanal. Chem.*, 2022, **920**, 116633.
- 8 A. Xie, J. Zhang, X. Tao, J. Zhang, B. Wei, W. Peng, Y. Tao and S. Luo, *Electrochim. Acta*, 2019, **324**, 134814.
- 9 M. Yang, H. Zhu, Y. Zheng, C. Zhang, G. Luo, Q. Xu, Q. Li, S. Zhang, T. Goto and R. Tu, *RSC Adv.*, 2022, **12**, 10496–10503.
- 10 D. Xu, C. Mu, B. Wang, J. Xiang, W. Ruan, F. Wen, X. Du, Z. Liu and Y. Tian, *Sci. China Mater.*, 2017, **60**, 947–954.
- 11 V. D. Silva, R. A. Raimundo, T. A. Simões, F. J. A. Loureiro, D. P. Fagg, M. A. Morales, D. A. Macedo and E. S. Medeiros, *Int. J. Hydrogen Energy*, 2021, **46**, 3798–3810.
- 12 E. Omurzak, J. Jasnakunov, N. Mairykova, A. Abdykerimova, A. Maatkasymova, S. Sulaimankulova, M. Matsuda, M. Nishida, H. Ihara and T. Mashimo, *J. Nanosci. Nanotechnol.*, 2007, **7**, 3157–3159.
- 13 S.-J. Kim, B. H. Kim, M. C. Chung, H.-G. Ahn, S.-C. Kim, H.-G. Kim and S.-C. Jung, *J. Nanosci. Nanotechnol.*, 2013, **13**, 1997–2000.
- 14 Z. Kelgenbaeva, E. Omurzak, S. Takebe, S. Sulaimankulova, Z. Abdullaeva, C. Iwamoto and T. Mashimo, *J. Nanopart. Res.*, 2014, **16**, 2603.
- 15 H. Lee, S. H. Park, S.-C. Jung, J.-J. Yun, S.-J. Kim and D.-H. Kim, *J. Mater. Res.*, 2013, **28**, 1105–1110.
- 16 H.-G. Kim, H. Lee, B. H. Kim, S.-J. Kim, J.-M. Lee and S.-C. Jung, *Jpn. J. Appl. Phys.*, 2013, **52**, 01AN03.
- 17 H. Lee, S. H. Park, S.-G. Seo, S.-J. Kim, S.-C. Kim, Y.-K. Park and S.-C. Jung, *Curr. Nanosci.*, 2014, **10**, 7–10.
- 18 A. Alsaedi and Y. Show, *Nanomater. Nanotechnol.*, 2019, **9**, 1847980419853159.
- 19 X. Hu, O. Takai and N. Saito, *Jpn. J. Appl. Phys.*, 2013, **52**, 01AN05.
- 20 H. Lee, B.-J. Kim, Y.-K. Park, J.-S. Kim and S.-C. Jung, *Catal. Today*, 2020, **355**, 435–442.
- 21 L. Chen, C. Iwamoto, E. Omurzak, S. Takebe, H. Okudera, A. Yoshiasa, S. Sulaimankulova and T. Mashimo, *RSC Adv.*, 2011, **1**, 1083–1088.
- 22 L. Chen, T. Mashimo, E. Omurzak, H. Okudera, C. Iwamoto and A. Yoshiasa, *J. Phys. Chem. C*, 2011, **115**, 9370–9375.
- 23 W. Ma, T. Mashimo, S. Tamura, M. Tokuda, S. Yoda, M. Tsushida, M. Koinuma, A. Kubota, H. Isobe and A. Yoshiasa, *Ceram. Int.*, 2020, **46**, 26502–26510.
- 24 X. Hu, X. Zhang, X. Shen, H. Li, O. Takai and N. Saito, *Plasma Chem. Plasma Process.*, 2014, **34**, 1129–1139.
- 25 Z. Abdullaeva, E. Omurzak, C. Iwamoto, H. S. Ganapathy, S. Sulaimankulova, C. Liliang and T. Mashimo, *Carbon*, 2012, **50**, 1776–1785.
- 26 L. Chen, T. Mashimo, C. Iwamoto, H. Okudera, E. Omurzak, H. S. Ganapathy, H. Ihara, J. Zhang, Z. Abdullaeva, S. Takebe and A. Yoshiasa, *Nanotechnology*, 2013, **24**, 045602.
- 27 Z. Abdullaeva, E. Omurzak, C. Iwamoto, H. Okudera, M. Koinuma, S. Takebe, S. Sulaimankulova and T. Mashimo, *RSC Adv.*, 2013, **3**, 513–519.
- 28 W. Yu, H. Xie, L. Chen, Y. Li and C. Zhang, *Nanoscale Res. Lett.*, 2009, **4**, 465–470.
- 29 L. Lei, Z. Yao, J. Zhou, W. Zheng, B. Wei, J. Zu and K. Yan, *Carbon*, 2021, **173**, 69–79.
- 30 M. Chu, L. Wang, X. Li, M. Hou, N. Li, Y. Dong, X. Li, Z. Xie, Y. Lin, W. Cai and C. Zhang, *Electrochim. Acta*, 2018, **264**, 284–291.
- 31 M. Thommes, K. Kaneko, A. V. Neimark, J. P. Olivier, F. Rodriguez-Reinoso, J. Rouquerol and K. S. W. Sing, *Pure Appl. Chem.*, 2015, **87**, 1051–1069.
- 32 Y. Zheng, H. Deng, H. Feng, G. Luo, R. Tu and L. Zhang, *J. Colloid Interface Sci.*, 2023, **629**, 610–619.
- 33 Q. Chen, J. Li and Y. Li, *J. Phys. D: Appl. Phys.*, 2015, **48**, 424005.
- 34 M. S. Benilov, *J. Phys. D: Appl. Phys.*, 2008, **41**, 144001.
- 35 H. Hoelt and T. Huiskamp, *Eur. Phys. J. D*, 2018, **72**, 217.
- 36 S. Nijdam, J. Teunissen and U. Ebert, *Plasma Sci. Technol.*, 2020, **29**, 103001.
- 37 B. R. Locke and S. M. Thagard, *Plasma Chem. Plasma Process.*, 2012, **32**, 875–917.



- 38 Y. Liu, G. Mou, Y. Wang, F. He, N. Dong, Y. Lin, M. Zhong and B. Su, *ACS Appl. Nano Mater.*, 2022, **5**, 2953–2961.
- 39 B. Su, Y. Wang, H. Luo, M. Zhong and Z. Lei, *Part. Part. Syst. Charact.*, 2020, **38**, 2000268.
- 40 Y. Li, J. Huang, G. Rao, C. Wu, X. Du, Y. Sun, X. Wang and C. Yang, *Appl. Surf. Sci.*, 2020, **530**, 147192.
- 41 Z. Zhang, S. Liu, F. Xiao and S. Wang, *ACS Sustainable Chem. Eng.*, 2016, **5**, 529–536.
- 42 A. S. Singh, D. N. Srivastava and A. V. Biradar, *ACS Appl. Energy Mater.*, 2022, **5**, 14945–14956.
- 43 I. Elizabeth, A. K. Nair, B. P. Singh and S. Gopukumar, *Electrochim. Acta*, 2017, **230**, 98–105.
- 44 J. Wang, Z. Wu, L. Han, C. Xuan, J. Zhu, W. Xiao, J. Wu, H. L. Xin and D. Wang, *Sustainable Energy Fuels*, 2017, **1**, 823–831.
- 45 L. Tan, A. Zhang, Z. Liu, P. a. Wei, P. Yang, H. Guo, H. Fang, J. Han, Y. Zhu and Z. Ren, *RSC Adv.*, 2021, **11**, 11779–11785.
- 46 H. Xu, X. Zhou, X. Lin, Y. Wu, X. Lin and H.-J. Qiu, *ACS Appl. Mater. Interfaces*, 2021, **13**, 54951–54958.
- 47 N.-T. Suen, S.-F. Hung, Q. Quan, N. Zhang, Y.-J. Xu and H. M. Chen, *Chem. Soc. Rev.*, 2017, **46**, 337–365.

